

PAPER • OPEN ACCESS

Microsputterer with integrated ion-drag focusing for additive manufacturing of thin, narrow conductive lines

To cite this article: Y S Kornbluth *et al* 2018 *J. Phys. D: Appl. Phys.* **51** 165603

View the [article online](#) for updates and enhancements.

Related content

- [Topical Review](#)
Davide Mariotti and R Mohan Sankaran
- [The 2017 Plasma Roadmap: Low temperature plasma science and technology](#)
I Adamovich, S D Baalrud, A Bogaerts *et al.*
- [Engineering metallic nanostructures for plasmonics and nanophotonics](#)
Nathan C Lindquist, Prashant Nagpal, Kevin M McPeak *et al.*



IOP | ebooks™

Bringing you innovative digital publishing with leading voices to create your essential collection of books in STEM research.

Start exploring the collection - download the first chapter of every title for free.

Microsputterer with integrated ion-drag focusing for additive manufacturing of thin, narrow conductive lines

Y S Kornbluth¹, R H Mathews², L Parameswaran², L M Racz²
and L F Velásquez-García^{3,4}

¹ Department of Mechanical Engineering, Massachusetts Institute of Technology, 77 Massachusetts Ave., Cambridge, MA 02139, United States of America

² MIT Lincoln Laboratory, 244 Wood St., Lexington, MA 02421, United States of America

³ Microsystems Technology Laboratories, Massachusetts Institute of Technology, 77 Massachusetts Ave., Cambridge, MA 02139, United States of America

E-mail: Velasquez@alum.mit.edu

Received 30 November 2017, revised 26 February 2018

Accepted for publication 7 March 2018

Published 4 April 2018



Abstract

We report the design, modelling, and proof-of-concept demonstration of a continuously fed, atmospheric-pressure microplasma metal sputterer that is capable of printing conductive lines narrower than the width of the target without the need for post-processing or lithographic patterning. Ion drag-induced focusing is harnessed to print narrow lines; the focusing mechanism is modelled via COMSOL Multiphysics simulations and validated with experiments. A microplasma sputter head with gold target is constructed and used to deposit imprints with minimum feature sizes as narrow as $9\ \mu\text{m}$, roughness as small as 55 nm, and electrical resistivity as low as $1.1\ \mu\Omega \cdot \text{m}$.

Keywords: additive manufacturing, interconnects, ion-drag focusing, microplasma, microsputterer

(Some figures may appear in colour only in the online journal)

1. Introduction

Additive manufacturing (AM) is the layer-by-layer fabrication of solid objects using a computer-aided design (CAD) file [1]. Over the past 30 years, AM has developed into a capability that offers unprecedented control over the shape of objects [2]. Today, we are beginning to gain control over composition and microstructure in order to achieve improved physical properties [3, 4]. However, we are limited in our ability to design material *function* directly [5] because we do not yet have the ability to print metals and semiconductors in multi-material

constructs that approach the properties of conventionally manufactured electronics.

As a first step towards this vision, we demonstrate the printing of microelectronics-quality interconnects—this capability alone has the potential to revolutionize the design and fabrication of complex microsystems. State-of-the-art microelectronic devices have metal interconnects made from sputtered thin films that are patterned using photolithography and subtractive processes e.g. plasma etching. While the combination of lithography and etching is highly effective in mass-producing massively multiplexed features with resolution of tens of nanometres [6], it is an expensive process requiring large capital outlay, increasingly beyond the reach of all but the largest companies. The need to design expensive static masks that must be produced anew for every design makes conventional back-end metal processes unsuitable for rapid prototyping and vulnerable to hacking. Further, conventional

⁴ Author to whom any correspondence should be addressed.



Original content from this work may be used under the terms of the [Creative Commons Attribution 3.0 licence](https://creativecommons.org/licenses/by/3.0/). Any further distribution of this work must maintain attribution to the author(s) and the title of the work, journal citation and DOI.

lithographic processes are limited to planar substrates. The ability to print microelectronics-quality interconnects enables the creation of custom, non-planar form factors for power and communications interfaces, enables structural electronics, provides an efficient method for rework, and provides a means to include ‘mass customized’ security features.

Researchers are currently investigating a wide range of approaches for AM of metal interconnects, with the goal of achieving small feature size, low resistivity, compatibility with a large set of printable materials, and simplicity in the manufacturing process (figure 1). Recent reports have focused on metal transfer techniques, e.g. the deposition of metallic nanoparticles and nanodroplets via extrusion [3, 7] and atomization of suspensions [8], extrusion of thermoplastics [9], electrospray printing [10], laser-assisted electrophoretic deposition [11], and laser-induced forward transfer [12], as well as *in situ* synthesis of metals, e.g. meniscus-confined electroplating [13], electroplating of locally dispensed ions in a liquid feedstock [14], laser-induced photo-reduction [15], and focused electron/ion beam-induced deposition [16]. In addition, there are reports of interconnects made of bulk metal thin wires embedded in a polymer matrix [17]. The reader is directed to the excellent article by Hirt *et al* [18] for a comprehensive review of these and other methods for producing fine-geometry metal structures via AM. The most developed of these techniques is arguably nanoparticle ink extrusion, where a silver nanoparticle liquid suspension, or ink, is extruded from a nozzle onto a substrate surface; the carrier solvent is evaporated afterwards during an annealing post-processing step, leaving a deposit made of nanoparticles with high electrical conductivity [7]. Careful formulation of the ink allows for stable formation of freestanding 3D objects. Over a decade of research into this path has resulted in its implementation in a commercially available metal 3D printing system [19]. However, nanoparticle ink extrusion is currently limited to silver; in addition, the method requires annealing at 250 °C, which limits the underlying substrate to materials compatible with this thermal budget.

Microplasma sputtering is a promising approach for additively manufactured interconnects that harnesses the same physical deposition process used in state-of-the-art microelectronics [20, 21]. However, it operates at a different length scale to directly deposit features without photolithographic patterning. The technique is also applicable to a wide material set that includes metals, semiconductors and insulators, all required to realize the vision of directly designed and printed function.

Sputtering is a physical deposition process in which a plasma, i.e. a quasi-neutral ionized gas, generates a shower of individual atoms ejected from a target to land on a substrate, producing a conformal coating. In its most basic configuration, a sputter reactor has two electrodes, i.e. a target electrode comprising the material to be deposited, and an anode electrode that is used to bias a voltage (the target is at a lower potential than the anode) to strike a plasma between the electrodes. The electric field between the electrodes accelerates the plasma’s ions towards the target; if a given ion has sufficient energy [22–24], it strikes the target with enough force to

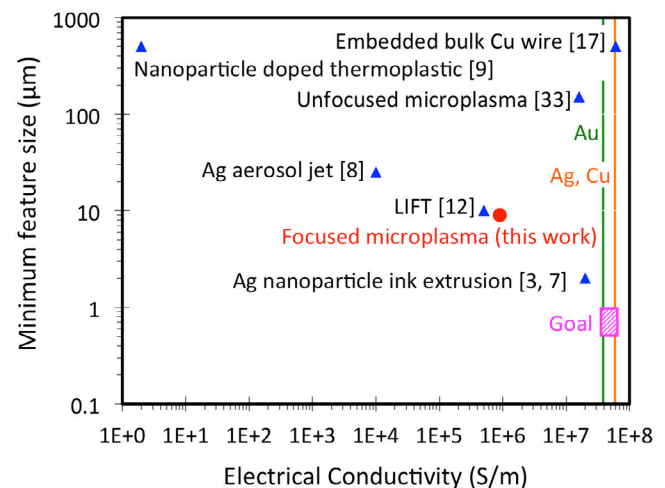


Figure 1. Minimum feature size versus electrical conductivity of reported additively manufactured conductive lines and this work (focused microplasma). Narrow, highly electrically conductive lines are of interest for producing microelectronics interconnects.

eject an atom approximately normal to the target surface with a fraction (~ 1 eV) of the incident ion’s energy. The stream of sputtered atoms moves away from the target to the anode and impinges on a substrate placed at some distance from the target, forming a solid deposit, i.e. film. If the sputtered material is a metal, the atom-by-atom creation of the deposit results in a continuous, conformal film with high electrical conductivity approaching that of the bulk material.

Sputtering in the microelectronics industry is done in large high-vacuum chambers (base pressure $\sim 10^{-6}$ Torr, operating pressure $\sim 10^{-3}$ Torr), where thin, flat semiconductor substrates are coated with thin, uniform films; sputtered metal thin films are patterned via photolithography and etching to form interconnects. The need for vacuum to produce ions can be obviated by reducing the dimensions of the plasma. Paschen discovered that the breakdown voltage of a gas, and similarly, much of the plasma’s behaviour, is a function of the product of the pressure and the distance between the electrodes, showing a minimum on the order of a few Torr · cm [25]. If a plasma is created at high pressure using a reactor of standard dimensions, the glow discharge produced is unstable, quickly transitioning to an arc discharge; however, by constraining plasmas to sub-millimetre lengths in one or more dimensions, it is possible to sustain stable plasmas at higher pressure, e.g. atmospheric pressure [26, 27]. Microplasmas have been used in a wide range of applications including mass spectroscopy [28], medical sterilization [29], processing of heat-sensitive polymers [30], excimer sources [31], and nanoparticle synthesis [32].

There are only a few recent scientific reports of atmospheric-pressure microplasma sources used to deposit metal. For example, Burwell [33] demonstrated printed gold lines using an argon microplasma generated with a target gold wire cathode surrounded by a ring anode; the author reported 150 μm wide lines with electrical conductivity approximately a third of that of the bulk metal without post-deposition annealing. Moreover, Abdul-Wahed *et al* [34, 35] used a nitrogen microplasma generated between a flat substrate and a copper target wire; by controlling the current of the plasma

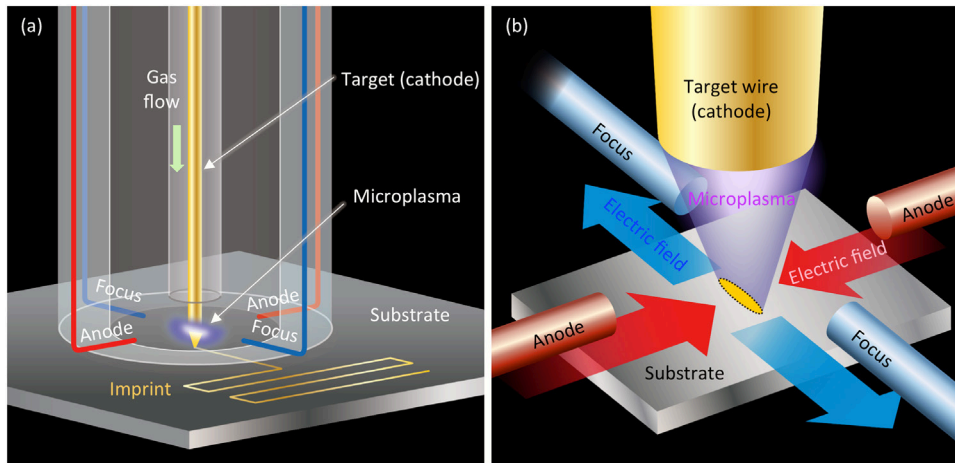


Figure 2. Schematic of the printhead as a metal line is being deposited (a); close-up schematic of printhead tip showing a focused imprint spot that is narrower in the direction between the anode electrodes (b).

diode, the deposit traced the footprint of the micromachined target on the substrate. While the reported work is promising, it is largely empirical, with little exploration of the parameter space; in addition, none of these reports addresses the incorporation of focusing to reduce the feature size of the deposits or is geared for continuous printing of the conductive material.

Focusing of the sputtered atom stream is critical to achieve features with geometries approaching those found in microelectronic circuits. Sputtered atoms travel nearly tangent to the normal of the target surface. In vacuum, the atoms travel from the target to the substrate with minimal scattering; however, at atmospheric pressure the sputtered atoms are buffeted by gas molecules, which causes spreading of the stream of sputtered material. Therefore, an unfocused microplasma printer can only produce imprints as narrow as the size of its target, with wider features generated as the separation between target and substrate is increased. In this study, we report a proof-of-concept demonstration of a novel, continuously fed microplasma metal sputterer that uses ion-drag focusing to print highly conductive lines narrower than the width of the target, without post-processing or photolithographic patterning. The focusing mechanism is described and validated via finite element simulations and experiments that explore the parameter space. Characterization of imprints deposited using a gold target was conducted, resulting in deposits with minimum feature size and resistivity that compare well with the state of the art.

2. Modelling

2.1. Proposed microplasma focusing approach

The architecture of the proposed microplasma reactor, i.e. *printhead*, is shown in figure 2. The printhead has a grounded central wire, i.e. *target*, surrounded by two pairs of electrodes evenly distributed around it: two opposing electrodes biased at a positive voltage, i.e. *anode electrodes*, that form the plasma, alternated by two opposing electrodes biased at a negative voltage, i.e. *focus electrodes*, that indirectly focus the plasma. The region of plasma near the target is the cathode

fall, characterized by a non-zero electrical field and a positive charge density.

By adjusting the placement of the electrodes, the electrostatic fields can be shaped to guide the plasma ions towards a localized spot on the substrate. As in ion vacuum pumps [36, 37] and electric-field induced combustion [38, 39], the ions collide with neutral gas atoms and, crucially, with sputtered metal atoms. Due to the relatively high pressures involved, molecular dynamics can be ignored and the collisions can be modelled as a net force that indirectly guides the metal atoms towards a focused spot on the substrate. This ion-drag focusing not only mitigates the problems caused by collisions, but also improves on a system under vacuum. In the absence of collisions, the printed line will be at least as wide as the target; however, by focusing the sputtered material, it is possible to define features narrower than the width of the target. Ion vacuum pumps harness a similar method, but they draw the particles towards the electrodes, rather than towards an uncharged substrate. With optics, we can achieve the same effect without placing electrodes directly on or under our substrate.

Electrostatic focusing is a common technique in charged particle optics (CPO) [40]. However, the focusing of the microplasma sputterer differs from traditional CPO in a crucial way. In CPO charged particles move in vacuum, i.e. the only significant forces acting on the particles are electrostatic, greatly simplifying computation and allowing for focusing in point-like spots. In contrast, in the proposed focusing approach charged particles interact with a gas at atmospheric pressure, limiting the amount of focusing that can be achieved. If the gas is ion-drag focused onto a single point on a substrate, pressure will build up, forcing the focused gas to spread out. The impossibility of point focusing in this approach can be derived from the steady-state conservation of mass equation [26]

$$\nabla \cdot (\rho \vec{u}) = \rho \nabla \cdot \vec{u} + \vec{u} \cdot \nabla \rho = 0; \quad (1)$$

in cylindrical coordinates with rotational symmetry, equation (1) is equivalent to

$$\rho \left[\frac{\partial u_r}{\partial r} + \frac{u_r}{r} + \frac{\partial u_z}{\partial z} \right] = -u_r \frac{\partial \rho}{\partial r} - u_z \frac{\partial \rho}{\partial z} \quad (2)$$

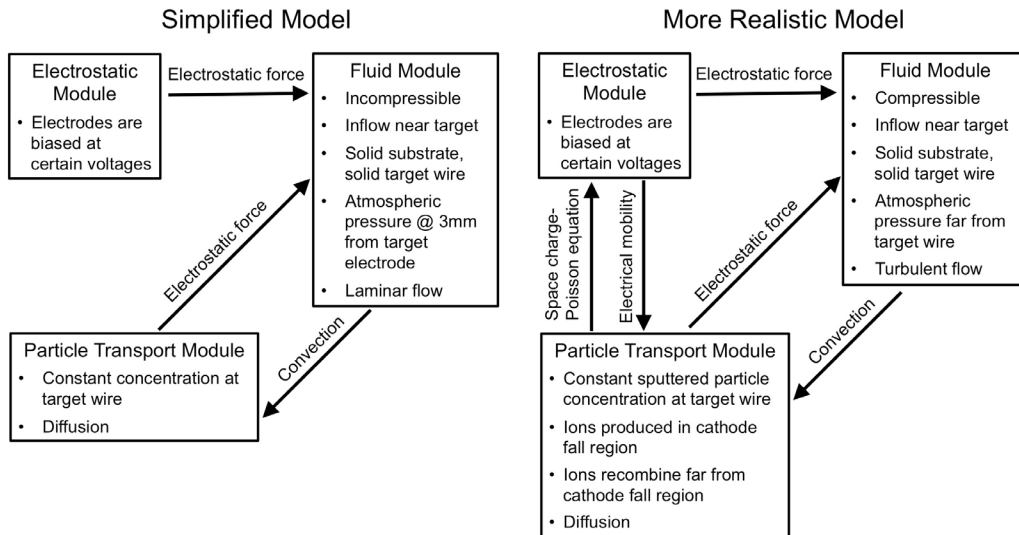


Figure 3. Schematic of the interaction of the three modules that compose the implemented simplified plasma model (left), and a more accurate plasma model for comparison (right). In the implemented model, the electric field has no dependencies, greatly simplifying calculations; in reality, the electric fields depend on the charge density. In both models, the transport of ions and the movement of the gas are coupled.

where u is the velocity of the gas, z is the distance from the target to the substrate, and r is the radial direction. For the left-hand side of equation (2) to be finite, u_r needs to vanish at $r = 0$; in addition, the presence of a solid surface that does not adsorb gas requires the boundary condition of $u_z = 0$ at the substrate. Consequently, the right-hand side of equation (2) must equal 0 at the substrate. However, for beam focusing to be viable u_r must be negative for small r , and u_z must be positive near the substrate, for the gas to carry the sputtered material to its surface. Therefore, the left-hand side in equation (2) must be negative, leading to a contradiction. The proposed ion-drag focusing scheme can bypass this limitation by focusing the stream of particles into a narrow line instead of a point because there is no pressure build-up when the gas is constrained in only one dimension. Beam line focusing is achieved by using the previously described two pairs of electrodes: the plasma is pushed away from the anode electrodes, while the focus electrodes pull the plasma towards them (in fact defocusing the plasma in that direction). A benefit of this focused beam profile is that it produces long and narrow lines required for interconnects. The expected degree of ionization of the plasma should not cause electric field shielding due to space charge within the plasma jet.

The proposed focusing approach clearly has trade-offs. As helpful as molecular collisions are to focusing, the sputtered atoms can collide with the gas and, after enough collisions, lose their initial momentum towards the substrate; the sputtered target atoms can redeposit on the target, coat the electrodes, or stick to any other surface of the printhead. Gas flow is introduced around the target wire to ensure that the majority of the sputtered material reaches the substrate, rather than straying off course due to collisions with the ambient atmosphere. The gas flow also dissipates heat produced by the plasma, preventing melting of the target wire.

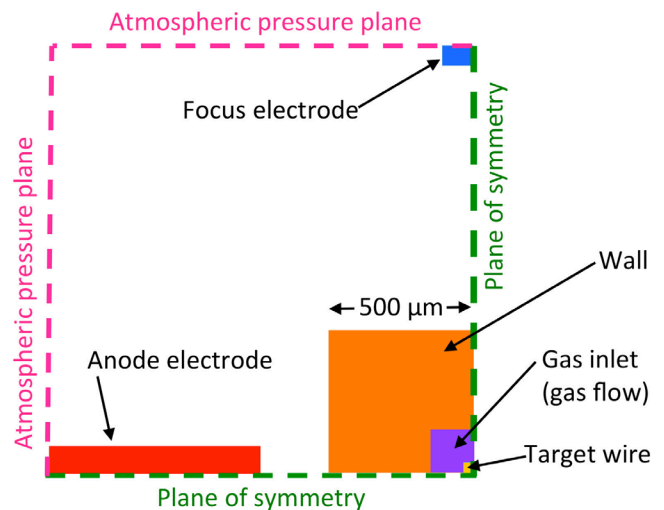


Figure 4. Top view of the geometry simulated, i.e. the upper left quadrant of the space between printhead tip and the substrate. The region is bounded by two planes of symmetry, the substrate, and two 3 mm-long walls at atmospheric pressure. Three electrodes (anode, focus, and target), biased at certain voltages, are placed at the top surface of the region of simulation. The substrate (not shown) is on the bottom of the simulated geometry.

2.2. Microplasma modelling

Plasmas, especially those at atmospheric pressure, are, in general, difficult to model due to the many interacting electromagnetic and hydrodynamic effects. Although there has been much work in atmospheric plasma modelling, most of this effort has concentrated on 1D and 2D, e.g. axisymmetric, systems [26, 27, 41–45]. However, in our application, modelling of the third dimension is essential. Therefore, a simplified 3D plasma fluid model [26] of the microsputterer reactor with ion-drag focusing, which sacrifices some of the detail common to other microplasma

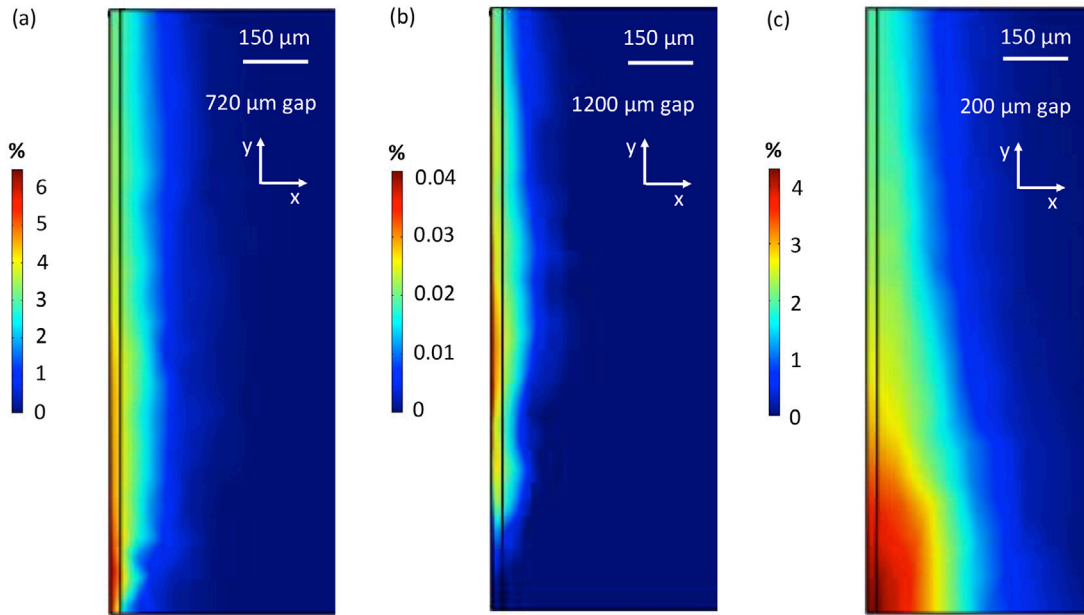


Figure 5. Concentration of sputtered material on the substrate for optimally focused (a) and non-optimally focused (b), (c) beams; concentration is normalized to the concentration at the target wire and is proportional to the thickness deposition rate at each point. Due to symmetry, only one quarter of the substrate is shown. Note the narrow width of the deposits, as evidenced by the black vertical line $25\ \mu\text{m}$ from the left edge on each plot that marks the boundary of the target wire. The x -direction runs between the anode electrodes, while the y -direction runs between the focus electrodes. (a) An imprint significantly narrower than the target; in contrast, (b) very low yield due to an overly large gap, and (c) a deposit wider than the target due to a decreased gap between the substrate and target. These simulations were run with anode bias voltage equal to 1 kV, focus bias voltage equal to $-750\ \text{V}$, and a gas flow rate of 33 sccm.

modelling by removing some of the phenomena that greatly increase the computational difficulty, was implemented in COMSOL Multiphysics. In this way, we follow in the footsteps of other models of ionic drag that similarly begin with a full plasma model and remove some of the more computationally challenging components [39, 41]. The steady-state model consists of three coupled modules (figure 3):

- The first module is an electrostatic calculator that solves Poisson's equation for a given spatial configuration of electrodes and bias voltages. The electric potential is assumed to be independent of the relatively small space charge in the regions of interest, greatly simplifying the problem.
- The second module is an incompressible laminar fluid flow solver. The flow field solution depends on the initial gas flow through the printhead and the positioning of the solid substrate with respect to the target.
- The third module deals with particle transport and ionic drag, that is, it tracks the movement of a solute through the space between the tip of the printhead and the substrate. The solute comprises both the net charge, which is greatest near the cathode electrode, and the sputtered metal, which originates at the cathode surface [23]. In our simplified model, these two physical quantities are proportional to each other, allowing us to track them together. Solute movement is primarily driven by convection, although some diffusion does occur. It is assumed that the collisions between molecules (with sub-micron mean free path) transform the electrostatic force on the ions to a volume force that acts on nearby gas molecules, neutral and charged alike. Therefore, the volume force on

the entire gas is proportional to the product of the electric field and the solute (charge) density.

The simplified model was implemented in a rectilinear one-quadrant geometry, i.e. a quadrant of the space between the tip of the printhead and the substrate, taking advantage of symmetry (figure 4). The dimensions of the microplasma nozzle were set based on designs in the literature [26, 27, 45] and geometry constraints of the available nozzle materials. Focus and anode electrodes are represented as rectangular regions some distance away from the target wire; the focus and anode electrodes are on the same plane, but the anode electrode is closer to the target than the focusing electrode. Gas flows through a $300\ \mu\text{m}$ diameter inlet surrounding the $50\ \mu\text{m}$ diameter target wire; a solid tube wall surrounds the inlet. The target-to-substrate separation is variable.

Selected results of the COMSOL modelling are shown in figure 5 (imprint formed at the substrate plane), figure 6 (ion-drag focusing of the imprint as the beam advances from the target to the substrate), and figure 7 (sputtering yield and center of mass of imprint formed at the substrate). For a suitable set of parameters (e.g. target-to-substrate separation, anode voltage, focus voltage) lines narrower than $20\ \mu\text{m}$ (full width at half maximum, i.e. FWHM) are predicted, with a yield (i.e. fraction of sputtered material that reaches the substrate) of 40% (figure 5). This high yield can be achieved, in part, due to the elongation of the deposit in one direction, allowing for a reasonable volumetric deposition rate despite a low thickness deposition rate. Given that the model is greatly simplified, no close match between the simulation results and the experimental data is expected; however, the model was

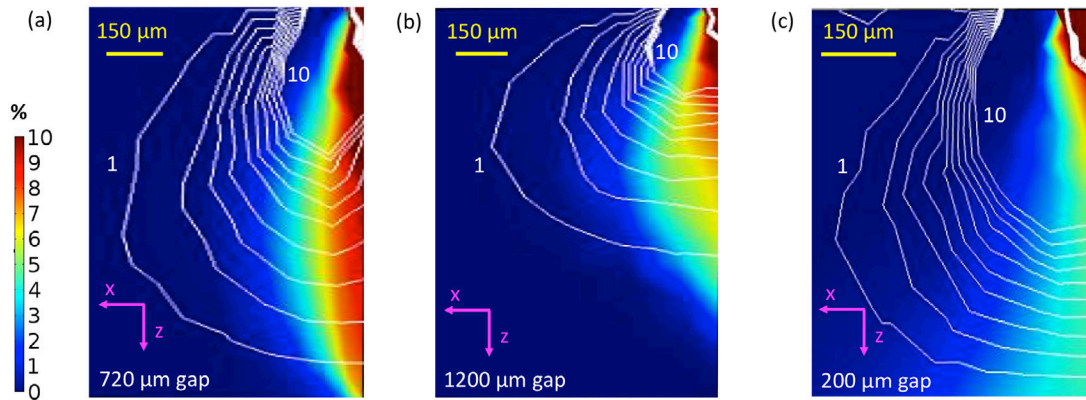


Figure 6. Side view of sputtered material concentration as the beam moves from target (top) to substrate (bottom). Optimally focused (a) and non-optimally focused (b) and (c) beams are shown, with the same parameters and concentration normalization used in figure 5; the x -direction runs between the anode electrodes, while the z -direction leads from the printhead to the substrate. The colour map is saturated at 10% of the concentration at the target to help visualization. White contour lines show the velocity of the gas flow towards the substrate every 1 m s^{-1} from 1 to 10 m s^{-1} . A scale bar for the horizontal direction is provided, while the total vertical dimension (i.e. target-to-substrate gap) in each plot is $720 \mu\text{m}$, $1200 \mu\text{m}$, and $200 \mu\text{m}$, respectively. With optimal focusing (a), the contour lines are roughly evenly spaced in the space directly in front of the target, and the sputtered material spreads (due to diffusion) before it focuses to a spot downstream from the target. (b) The sputtered material focuses above the substrate; because of the low gas flow rate near the substrate, most of the sputtered material does not reach the substrate. (c) Although some focusing is evident, there is not enough residence time for the flow to slow down; the pressure forces a sharp defocusing.

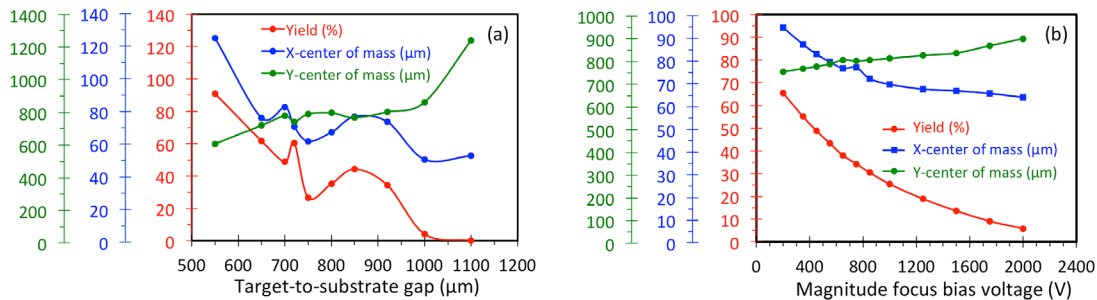


Figure 7. Yield and imprint center of mass in the x (anode-anode)- and y (focus-focus)-directions versus target-to-substrate gap (a) and magnitude of the (negative) focus bias voltage (b). As the substrate-to-target gap increases, less material reaches the substrate, although beam focusing improves. Similarly, a larger magnitude of focus bias voltage compresses the beam better, but also draws the gas flow towards the focus electrodes and away from the substrate, decreasing yield. (b) The center of mass in x decreases until the focus bias voltage is -750 V (signifying better focusing), but then begins to level off, suggesting that the optimal focus bias voltage for this set of parameters is -750 V . For each graph, the gas flow was held at 33 sccm ; in (a) focus bias voltage = -750 V , in (b) substrate-to-target gap = $920 \mu\text{m}$. The center of mass was measured for one quadrant of the imprint.

helpful to establish the following trends on how the different parameters influence the geometry of the imprints:

- The simulations show that optimal narrow lines with appreciable yields have associated gas flows in which the velocity towards the substrate decreases in an approximately linear fashion, with minimal slowing down due to pressure differentials. If the gas flow rate is too large (or, equivalently, if the target-to-substrate gap is too small), the gas travels at a very high velocity until it reaches the area of high pressure, resulting in insufficient residence time for the electrostatic forces to focus the gas flow before the hydrodynamic forces dominate (figure 6). If the gas flow rate is not large enough (or, equivalently, if the target-to-substrate gap is too large), convection is not able to carry the sputtered material to the substrate, diminishing the yield (figure 7(a)). This trend was confirmed by experiment.
- The anode bias voltage is set to maintain a stable plasma; in a typical experiment, the anode bias voltage was set around 1 kV (see section 3).

- The focus bias voltage also has an optimal value. A larger magnitude of the focus bias voltage improves focusing by pulling the plasma towards the focus electrodes and thus harnessing the hydrostatic pressure to decrease the line width. However, if the magnitude of the focus bias voltage is too large, the ions are drawn directly to the focus electrodes and never reach the substrate (figure 7(b)). In practice, the optimal value of the focus bias voltage is highly dependent on the gas flow rate but is of the same order of magnitude of the anode bias voltage.

3. Experimental apparatus and experimental procedure

A schematic and photographs of key components of the ion-drag-focused microspitter assembly, or printhead, are shown in figure 8. The microplasma printer uses a Thorlabs NRT 100 motorized translation stage to move the substrate relative to the printhead. Inputs to the printhead consist of gold wire

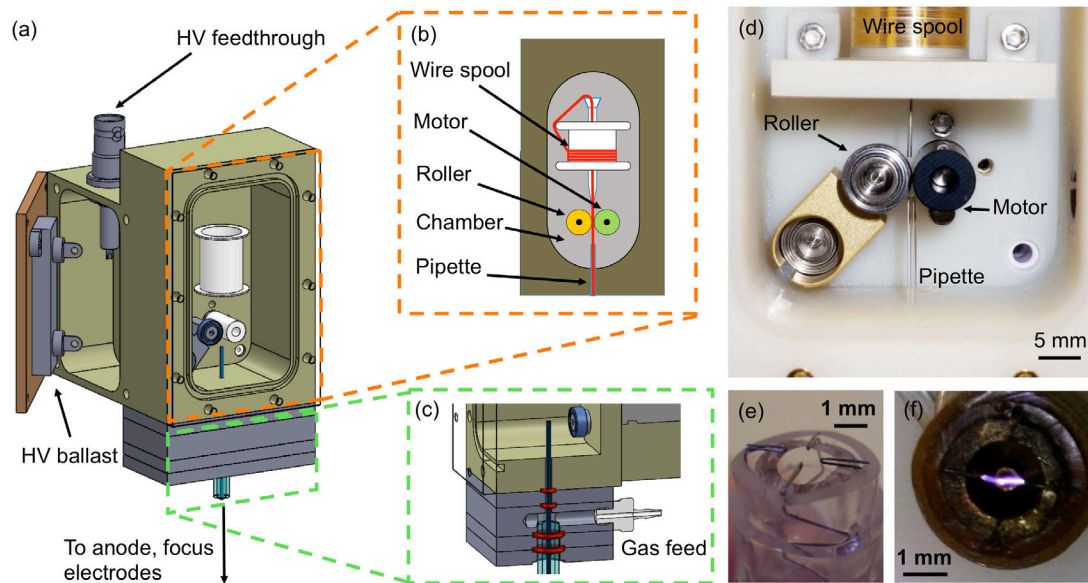


Figure 8. Schematic of the support system that supplies gas, electrical signals, and target wire to the printhead (a); schematic of target wire feed mechanism (b); cross-section schematic showing the gas feed (c); close-up of implemented wire feed mechanism (d); nozzle with electrode wires (e); plasma generated at nozzle tip (f). (f) The longer anode electrode pair generates the plasma and compresses the beam, while the focus electrode pair, perpendicular to the anode pair, is used to prevent pressure build-up.

(Sigma Aldrich, 50 μm diameter, purity >99.99%) acting as target feedstock, compressed dry air, and electrical signals. The target wire is continuously supplied to the printhead using a novel feed mechanism (figures 8(b) and (d)). The target wire sits on a spool, while a controlled (Micromo MCST 3601 motion controller) stepper motor (Faulhaber AM1524), capped by a rubber head, pushes the wire against a roller, incrementally feeding the wire to a pipette that connects to the printhead. The vertical separation between the printhead tip (nozzle) and the substrate is controlled with a Newport 433 ball bearing manual linear stage with an SM50 micrometer (50 mm of travel distance, 100 μm vernier resolution). Given that the voltage drop across the plasma increases as the inter-electrode distance increases, the anode bias voltage can be used as an indirect measurement of the separation between the tip of the printhead and the anode electrodes. In our setup, monitoring the anode voltage and actuating the stepper motor wire feed accordingly can ensure that the inter-electrode distance is constant to within 50 μm and the anode voltage is within 50 V of its target value.

The printhead nozzle has a set of four tungsten electrodes evenly distributed around the target, where opposite pairs act as the anode and focus bias electrodes as previously described in section 2 (figure 8(e)); tungsten was chosen due to its resistance to sputtering (undesired plasma formation between the anode and focus electrodes can cause electrode sputtering). The anode electrode pair is used to generate the plasma and compress the beam in one direction, while the focus pair expands the beam in the other direction, preventing pressure build-up (figure 8(f)). The anode pair is longer than the focus pair to prevent striking a plasma between them. A quartz substrate with laser-drilled holes was used to control the electrode position at the nozzle, allowing for a robust assembly with no electrode shorting.

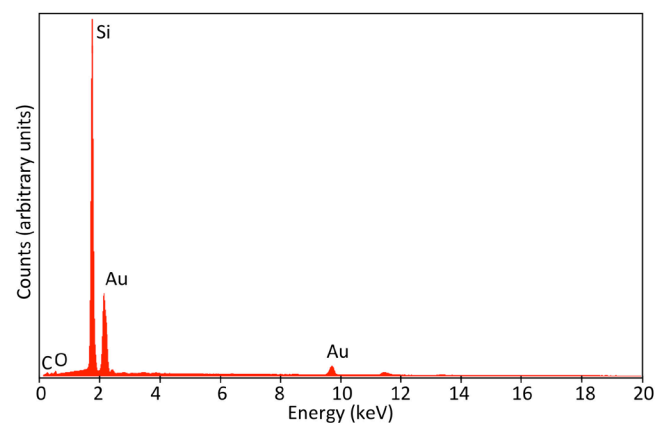


Figure 9. EDX analysis of an imprint. The primary elements seen are Si (from the substrate) and Au (from the deposit). Traces of O (from the silicon dioxide film underneath the imprint) and C (may be due to impurities on the wire or in the ambient air) are also visible.

All sputterers suffer from a loss of yield due to reflected sputtered material; atmospheric pressure sputterers are particularly affected by this problem due to the increased number of collisions with gas molecules, relative to vacuum sputterers. The proposed focusing mechanism helps alleviate this problem by guiding the sputtered material via ionic drag; also, reducing the target-to-substrate separation further mitigates this issue. However, the plasma will naturally form along the line of greatest potential gradient; if the substrate is conductive or is covered with a thin insulating layer (e.g. a silicon wafer coated with thermal oxide), a conductive path may lead from the focus electrodes to the substrate, along the substrate, and then from the substrate to the anodes, bypassing the target wire and damaging the substrate. Experimentally, we found that lowering the tip of the target wire to 100 μm below the plane of the anode/focus electrode pairs, closer to

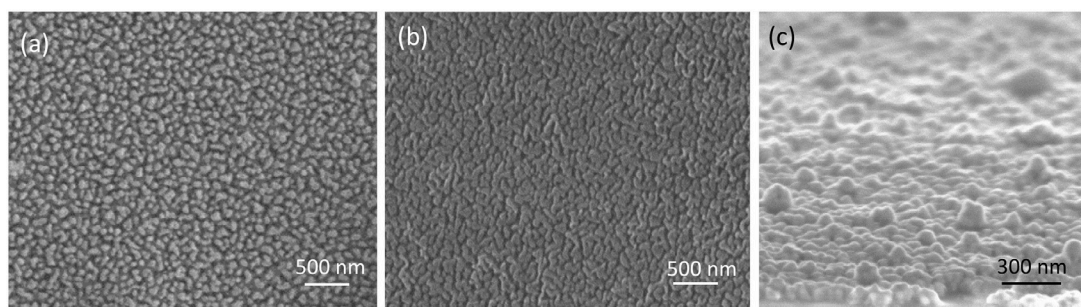


Figure 10. Scanning electron microscope images of imprints created without gas flow (a), and with 5 sccm of gas flow rate ((b) and (c)). Note the relatively small grains in (a)—electrical characterization of the deposit suggests the grains are disconnected. (b), (c) The grains form a compact, electrically conductive network with surface morphology, as seen in the tilted view in (c). Larger gas flow rate results in more uniform, connected films, although no further improvement in the grain structure was realized experimentally for flow rates greater than 5 sccm.

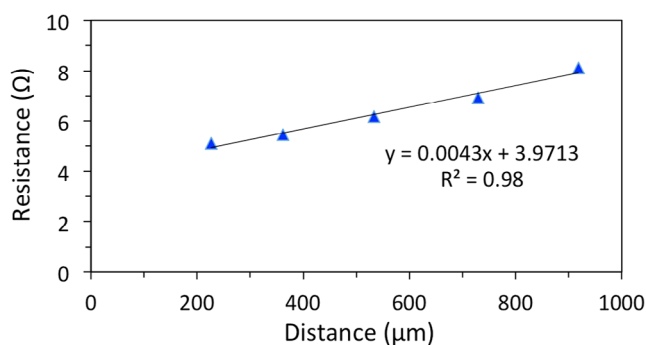


Figure 11. Electrical resistance versus probe separation. For each data point, the resistance was measured between two points on a straight line. The data are satisfactorily described by a linear fit; from the slope of the linear fit, an electrical resistivity equal to $1.1 \mu\Omega \cdot \text{m}$ ($0.75 \Omega \square^{-1}$) is estimated. The contact resistance is estimated at $\sim 2 \Omega$.

the substrate, sets a sufficiently small target-to-substrate gap, while still maintaining an electrode-to-substrate air gap that forces the plasma to form between the anodes and the tip of the target wire, avoiding the substrate. Given that a glass pipette surrounds the target wire, the plasma is forced to stretch below the plane of the anode/focus electrodes and anchor to the tip of the target wire. This configuration, in which the plasma anchors to the tip of the target, ensures that sputtered material will be ejected towards the substrate, not towards the sides of the printhead. The use of the glass pipette elongates the plasma's path, forcing the use of a larger anode bias voltage.

Compressed dry air is supplied to the printhead using a UFC 1000 mass flow controller with a supply range of 0–25 sccm. The anode bias voltage is regulated by a Keithley 2657A power supply. The power supply regulates the current, typically at a value between 0.1 and 1.5 mA. The resultant bias voltage, between 1 and 2.5 kV, flows through a $1 \text{ M}\Omega$ ballast resistor before reaching the anode electrodes. The focus bias voltage is regulated by a HP 7516A power supply, which supplies a constant voltage (relative to ground) and no current. Once the plasma is stable, the translation stage is actuated according to the experimental requirements. By using the wire feed mechanism, we have achieved continuous deposition times in excess of 6 h, with momentary stops to change parameters and substrates.

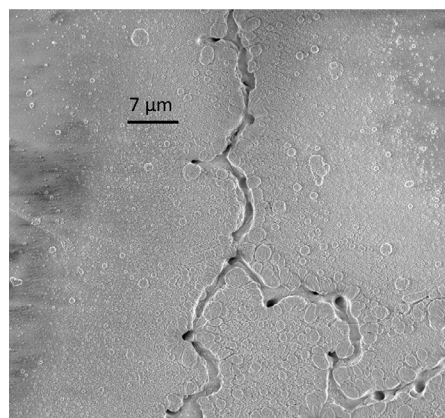


Figure 12. A cracked imprint. This sample is $2 \mu\text{m}$ thick; $1 \mu\text{m}$ -wide cracks appear at points of high mechanical stress.

4. Experimental results and discussion

Characterization of the microplasma-sputtered imprints included chemical analysis, film porosity, film roughness, electrical resistivity, and imprint metrology. Chemical analysis was done with an EDAX energy dispersive x-ray (EDX) analysis tool; imprint metrology was conducted with a Carl Zeiss 1525 field emission scanning electron microscope (porosity) and a Keyence VK-250 laser scanning confocal microscope (roughness and profiles); a combination of probe stations and test structures was used to measure electrical resistivity. Each of these characteristics is a function of the parameters used in the printing; where applicable, we describe the effects of the parameters.

4.1. Chemical composition imprints

EDX measurements show that the imprint is nearly entirely made of gold, with traces of carbon contamination (figure 9). The silicon and oxygen peaks present are from the silicon-dioxide-coated silicon substrate used to collect the imprint. Notably, even though we sputter in atmosphere, no nitrogen is trapped in the deposit. Also notable is the absence of tungsten, indicating that there is no spurious sputtered material from the electrodes.

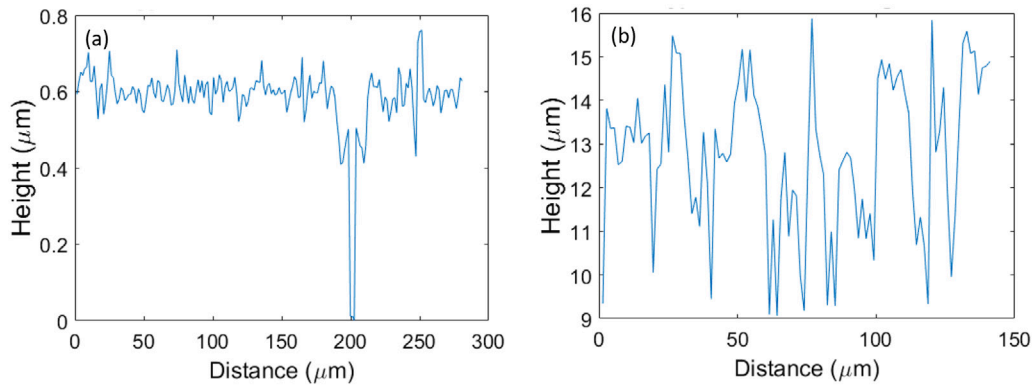


Figure 13. A 1D profile scan of a smooth deposit—created by a well-behaved plasma (a), and analogous scan of a rough deposit—created by a varying plasma (b). The roughness ranges from 55 nm in the former case to 2.48 μm in the latter case. Note the small void in the left profile, exposing the underlying substrate and showing that the thickness of the deposit is approximately 10 times the roughness.

4.2. Generation of non-porous films

Early deposition experiments without gas flow produced extremely porous imprints, which were electrically non-conductive (figure 10(a)). This result has been documented in the literature on sputter deposition at high pressures; some researchers attribute the highly porous morphology to the aggregation of sputtered atoms in the air before deposition [46], while others claim that a shadowing effect causes the sputtered particles to be blocked by extant deposits before they can reach the substrate [47, 48]. However, the same references agree that directed sputter deposition, in which the sputtered material retains its initial velocity, does not suffer from this problem, since the sputtered metal moves directly towards the substrate without being affected by collisions. Introduction of a flow of compressed dry air resulted in electrically conductive imprints—scanning electron microscope images of the samples reveal a visibly less porous structure (figure 10(b)).

4.3. Characterization of imprints' electrical conductivity

The electrical conductivity of the non-porous samples was characterized with multiple two-point resistance measurements along the imprint. Electrical resistivity is estimated to be 1.1 $\mu\Omega \cdot \text{m}$, which is 50 \times the bulk resistivity of gold (figure 11). This result is an order of magnitude worse than previous reports on microplasma-printed metal lines [33]; we hypothesize this is likely due to the higher gas flow rate used in those experiments (as described earlier, higher gas flow suppresses the formation of grain boundaries, decreasing porosity and increasing electrical conductivity). Given that the proposed ion-drag focusing approach works best with low gas flow rates, we speculate that increasing the electrical conductivity of the imprints without significantly increasing their feature size will require optimization of the flow rate, bias, and number of print passes. Alternatively, the significantly better electrical conductivity reported in [33] may be due to annealing (in such report, the substrate reached a temperature of 600 $^{\circ}\text{C}$ during deposition). Our substrate shows no significant temperature elevation, e.g. a thin film of LDPE, when placed on the substrate, did not soften; this suggests an upper bound on the substrate temperature near 100 $^{\circ}\text{C}$.

4.4. Thickness variation, roughness, deposition rate

Deposits 300 nm to 20 μm thick were produced. However, deposits that are both thick and narrow develop large cracks due to mechanical stresses in the film. These cracks can be visually distinguished from the grain boundaries (figure 12). The surface roughness of the samples, found by calculating the average arithmetical mean deviation over a typical 20000 μm^2 area, varies greatly, arguably due to variations in the plasma's behaviour. On the one hand, when the plasma is maintained in a steady state, i.e. without drastic changes in voltage or in its path between the electrodes, roughness as small as 55 nm has been observed (figure 13(a)); on the other hand, if the plasma significantly changes its behaviour over time, the roughness can be over an order of magnitude greater (figure 13(b)). Volumetric and thickness deposition rates are estimated at 200 $\mu\text{m}^3 \text{ s}^{-1}$ and 3.3 nm s^{-1} , respectively, i.e. a deposit $\sim 20 \mu\text{m}$ wide, 3 mm long, and 3 μm thick is printed in 15 min. This is comparable with other reports on microplasma printing when similar currents are used [33, 34]. Using a different set of parameters (e.g. higher gas flow and smaller target-substrate gaps) yielded volumetric deposition rates 10 times greater.

4.5. Focusing characterization

Without focusing, a roughly symmetric dot is deposited (figure 14(a)); these imprints tend to have a diameter on the order of hundreds of microns, although the size of the imprint varies with target-to-substrate gap, gas flow rate, and bias voltage. With focusing, a line width (FWHM) as small as 9 μm was obtained, i.e. less than one fifth the width of the target wire and more than an order of magnitude narrower than imprints from previous microplasma sputterers [34] (figure 14(c)). The line is well defined with very steep sidewalls and has a high length-to-width ratio, even with a stationary printhead during the deposition. COMSOL simulations predict that, as the gas flow rate increases and the target-to-substrate gap decreases, the yield increases and the focusing degrades; this prediction was tested by varying the target-to-substrate gap. The experimental results suggest that the prediction holds for gaps smaller than the ideal focusing gap; for large gaps, the yield decreased so much that it was impossible to accurately characterize the imprints.

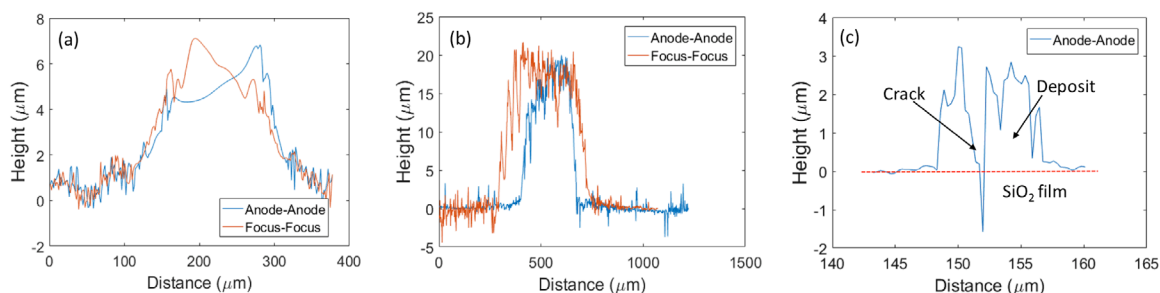


Figure 14. An unfocused (a), slightly focused (b), and highly focused (c) deposit; each deposit was created by running the printhead for 15 min. The unfocused deposit was produced without focus bias voltage (i.e. focus electrodes were left floating) and is roughly symmetrical. Significant asymmetry is apparent in the slightly focused deposit; the length of the imprint running from anode to anode is approximately $250\ \mu\text{m}$, while the length running from focus electrode to focus electrode is $410\ \mu\text{m}$. The highly focused deposit is $9\ \mu\text{m}$ wide and approximately $3\ \mu\text{m}$ thick; the deposit is cracked due to the stresses induced by the thickness of the deposit. The highly focused deposit is $3\ \text{mm}$ long; it was produced without moving the substrate relative to the printhead. The apparent propagation of the crack in the SiO_2 film is an artefact of the confocal microscopy measurement technique. (c) Only the scan of the width of the highly focused deposit is shown ($9\ \mu\text{m}$, anode-anode direction) because the length of the deposit ($3\ \text{mm}$, focus-focus direction) cannot be clearly shown on the same scale.

5. Conclusions and future work

A proof-of-concept demonstration of a continuously-fed microplasma metal sputterer with ion-drag focusing was demonstrated. The microsputterer is capable of printing highly electrically conductive lines narrower than the width of the target without the need for post-processing or lithographic patterning. Characterization of the imprints using a gold target was conducted; minimum feature sizes as narrow as $9\ \mu\text{m}$, roughness as small as $55\ \text{nm}$, and electrical resistivity as low as $1.1\ \mu\Omega \cdot \text{m}$ were obtained.

Although the reported work has not matched the performance of state-of-the-art conductive silver ink techniques [7], the results are competitive and have great potential for improvement. In this study, the electrical resistivity of the imprints is $\sim 20\times$ larger than the best results using conductive silver ink due to insufficient gas flow; however, theory and literature on metal microsputters [33] suggest that electrical resistivity values lower than those achieved with conductive inks are possible if an appropriate gas flow compatible with focusing is found. In addition, the smallest features achieved in this study are $\sim 5\times$ larger than the best results using conductive silver ink; nonetheless, through comprehensive computational investigation, it was determined that finer features are possible if the parameters of operation are carefully chosen. The data reported in this study did not involve any post-processing (e.g. annealing) or environmental control (e.g. relative humidity regulation), and the technique is compatible with other printable materials—all clear advantages over conductive silver ink techniques. Because of the insurmountable difficulties of quantitative plasma simulations, significant experimental exploration of the parameter space and further refinement of our methodologies and equipment will be required to achieve better performance.

Acknowledgments

This work is based upon work supported under US Air Force Contract No. FA8721-05-C-0002 and/or FA8702-15-D-0001.

Any opinions, findings, conclusions or recommendations expressed in this material are those of the authors and do not necessarily reflect the views of the US Air Force. The authors would like to thank Zhumei Sun, Velásquez Research Group, Massachusetts Institute of Technology, for her assistance with measurements.

ORCID iDs

Y S Kornbluth <https://orcid.org/0000-0001-7813-3784>
 L Parameswaran <https://orcid.org/0000-0002-5566-9495>
 L M Racz <https://orcid.org/0000-0002-1876-8566>
 L F Velásquez-García <https://orcid.org/0000-0002-9232-1244>

References

- [1] Wong K V and Hernandez A 2012 A review of additive manufacturing *ISRN Mech. Eng.* **2012** 208760
- [2] Lipson H 2012 The shape of things to come: frontiers in additive manufacturing *Bridge* **42** 5–12
- [3] Skylar-Scott M A, Gunasekaran S and Lewis J A 2016 Laser-assisted direct ink writing of planar and 3D metal architectures *Proc. Natl Acad. Sci. USA* **113** 6137–42
- [4] Qin Z, Jung G S, Kang M J and Buehler M J 2017 The mechanics and design of a lightweight three-dimensional graphene assembly *Sci Adv.* **3** e1601536
- [5] Olvera-Trejo D and Velásquez-García L F 2016 Additively manufactured MEMS multiplexed coaxial electro spray sources for high-throughput, uniform generation of core-shell microparticles *Lab Chip* **16** 4121–32
- [6] Campbell S A 2001 *The Science and Engineering of Microelectronic Fabrication* 2nd edn (New York: Oxford University Press)
- [7] Ahn B Y, Duoss E B, Motala M J, Guo X, Park S-I, Xiong Y, Yoon J, Nuzzo R G, Rogers J A and Lewis J A 2009 Omnidirectional printing of flexible, stretchable, and spanning silver microelectrodes *Science* **323** 1590–3
- [8] Maiwald M, Werner C, Zoellmer V and Busse M 2010 INKtelligent printed strain gauges *Sensors Actuators A* **162** 198–201

- [9] Sun Z and Velásquez-García L F 2017 Monolithic FFF printed, biodegradable, biocompatible, dielectric–conductive microsystems *J. Microelectromech. Syst.* **26** 1356–70
- [10] Yu J H, Kim S Y and Hwang J 2007 Effect of viscosity of silver nanoparticle suspension on conductive line patterned by electrohydrodynamic printing *Appl. Phys. A* **89** 157–9
- [11] Takai T, Nakao H and Iwata F 2014 Three-dimensional microfabrication using local electrophoresis deposition and a laser trapping technique *Opt. Exp.* **22** 28109–17
- [12] Germain C, Charron L, Lilje L and Tsui Y Y 2007 Electrodes for microfluidic devices produced by laser induced forward transfer *Appl. Surf. Sci.* **253** 8328–33
- [13] Hu J and Yu M-F 2010 Meniscus-confined three-dimensional electrodeposition for direct writing of wire bonds *Science* **329** 313–6
- [14] Hirt L, Ihle S, Pan Z, Dorwling-Carter L, Reiser A, Wheeler J M, Spolenak R, Vörös J and Zambelli T 2016 Template-free 3D microprinting of metals using a force-controlled nanopipette for layer-by-layer electrodeposition *Adv. Mater.* **28** 2311–5
- [15] Cao Y-Y, Takeyasu N, Tanaka T, Duan X-M and Kawata S 2009 3D metallic nanostructure fabrication by surfactant-assisted multiphoton induced reduction *Small* **5** 1144–8
- [16] Tasco V, Esposito M, Todisco F, Benedetti A, Cuscunà M, Sanvitto D and Passaseo A 2016 Three-dimensional nanohelices for chiral photonics *Appl. Phys. A* **122** 280
- [17] Espalin D, Muse D W, MacDonald E and Wicker R B 2014 3D printing multi-functionality: structures with electronics *Int. J. Adv. Manuf. Technol.* **72** 963–78
- [18] Hirt L, Reiser A, Spolenak R and Zambelli T 2017 Additive manufacturing of metal structures at the micrometer scale *Adv. Mater.* **29** 1604211
- [19] Lau G-K and Shrestha M 2017 Ink-jet printing of micro-electro-mechanical systems (MEMS) *Micromachines* **8** 194
- [20] Wasa K and Hayakawa S 1992 *Handbook of Sputter Deposition Technology* (Westwood, NJ: Noyes)
- [21] Behrisch R and Wittmaack K 1981 *Sputtering by Particle Bombardment* vol 1 (Berlin: Springer)
- [22] Yamamura Y, Matsunami N and Itoh N 1982 A new empirical formula for the sputtering yield *Radiat. Effects* **68** 83–7
- [23] Chapman B 1980 *Glow Discharge Processes: Sputtering and Plasma Etching* (New York: Wiley)
- [24] Oliva-Florio A, Baragiola R A, Jakas M M, Alonso E V and Ferrn J 1987 Noble-gas ion sputtering yield of gold and copper: dependence on the energy and angle of incidence of the projectiles *Phys. Rev. B* **35** 2198
- [25] Paschen F 1889 Ueber die zum Funkenübergang in Luft, Wasserstoff und Kohlensäure bei verschiedenen Drucken erforderliche Potentialdifferenz *Ann. Phys.* **273** 69–75
- [26] Papadakis A P, Rossides S and Metaxas A C 2011 Microplasmas: a review *Open Appl. Phys. J.* **4** 45–63
- [27] Schoenbach K H and Becker K 2016 20 years of microplasma research: a status report *Eur. Phys. J. D* **70** 1–22
- [28] Eijkel J C T, Stoeri H and Manz A 1999 A molecular emission detector on a chip employing a direct current microplasma *Anal. Chem.* **71** 2600–6
- [29] Schoenbach K H 2013 *High-Pressure Microcavity Discharges, in Low Temperature Plasma Technology: Methods and Applications* (Boca Raton, FL: CRC Press)
- [30] Araújo E C B B, Nascimento J C, Fernandes A D, Barbosa F T F, Sousa D C, Oliveira C, Abreu G J P, Ribas V W and Sismanoglu B N 2014 Low temperature microplasma jet at atmospheric pressure for inducing surface modification on polyethylene substrates *Am. J. Condens. Matter Phys.* **4** 1–7
- [31] Zhu W, Takano N, Schoenbach K H, Guru D, McLaren J, Heberlein J, May R and Cooper J R 2007 Direct current planar excimer source *J. Phys. D: Appl. Phys.* **40** 3896–906
- [32] Richmonds C and Sankaran R M 2008 Plasma-liquid electrochemistry: rapid synthesis of colloidal metal nanoparticles by microplasma reduction of aqueous cations *Appl. Phys. Lett.* **93** 131501
- [33] Burwell E 2016 A microplasma-based sputtering system for direct-write, microscale fabrication of thin-film metal structures *MS Thesis* Case Western Reserve University
- [34] Abdul-Wahed A M, Roy A L, Xiao Z and Takahata K 2016 Direct writing of thin and thick metal films via micro glow plasma scanning *Technical Digest 29th IEEE Conf. on Micro Electro Mechanical Systems* pp 443–6
- [35] Abdul-Wahed A M, Roy A L and Takahata K 2016 Microplasma drawing of thermocouple sensors *Technical Digest IEEE Sensors Conf. (Orlando, FL)* (<https://doi.org/10.1109/ICSENS.2016.7808951>)
- [36] Hall L D 1958 Electronic ultra-high vacuum pump *Rev. Sci. Instrum.* **29** 367–70
- [37] Grzebyk T, Knapkiewicz P, Szyszka P, Górecka-Drzazga A and Dziuban J A 2016 MEMS ion-sorption high vacuum pump *J. Phys.: Conf. Ser.* **773** 012047
- [38] Carleton F B and Weinberg F J 1987 Electric field-induced flame convection in the absence of gravity *Nature* **330** 635
- [39] Papac M J and Dunn-Rankin D 2008 Modelling electric field driven convection in small combustion plasmas and surrounding gases *Combust. Theory Modelling* **12** 23–44
- [40] Harting E and Read F H 1976 *Electrostatic Lenses* (New York: Elsevier)
- [41] Malik M, Weinstein L and Hussaini M 1983 Ion wind drag reduction *21st Aerospace Sciences Meeting 231* (<https://doi.org/10.2514/6.1983-231>)
- [42] Farouk T et al 2007 Modeling of direct current micro-plasma discharges in atmospheric pressure hydrogen *Plasma Sources Sci. Technol.* **16** 619
- [43] Hong Y J, Lee S M, Kim G C and Lee J K 2008 Modeling high-pressure microplasmas: comparison of fluid modeling and particle-in-cell Monte Carlo collision modeling *Plasma Processes Polym.* **5** 583–92
- [44] Wilson C G, Gianchandani Y B, Arslanbekov R R, Kolobov V and Wendt A E 2003 Profiling and modeling of DC nitrogen microplasmas *J. Appl. Phys.* **94** 2845–51
- [45] Becker K H, Schoenbach K H and Eden J G 2006 Microplasmas and Applications *J. Phys. D: Appl. Phys.* **39** R55
- [46] Carton O, Ghaymouni J, Lejeune M and Zeinert A 2013 Optical characterization of porous sputtered silver thin films *J. Spectrosc.* **2013** 307824
- [47] Oudrhiri-Hassani F, Presmanes L, Barnabe A and Tailhades P 2008 Microstructure, porosity and roughness of RF sputtered oxide thin films: characterization and modelization *Appl. Surf. Sci.* **254** 5796–802
- [48] Alvarez R, Garcia-Martin J M, Garcia-Valenzuela A, Macias-Montero M, Ferrer F J, Santiso J, Rico V, Cotrino J, Gonzalez-Elipe A R and Palmero A 2015 Nanostructured Ti thin films by magnetron sputtering at oblique angles *J. Phys. D: Appl. Phys.* **49** 045303